Bio-Design and Manufacturing (2025) 8:709–723
https://doi.org/10.1631/bdm.2400486

RESEARCH ARTICLE

Evaluation of the 3D printable temperature-responsive shape-memory PLTG terpolymers for minimally invasive surgery

Xulin Hu[1] · Jun Wang[2,3] · Shuhao Yang[2] · Jun Deng[4] · Wanyue Feng[1] · Haoming Wu[1] · Dongdong Han[1] · Leilei Qin[2] · Jianye Yang[2] · Zhengguang Pu[1] · Xin Yong[6] · Yanlin Li[3] · Shuai Li[5] · Ning Hu[2]

Received: 2 December 2024 / Accepted: 23 March 2025

Abstract

Three-dimensional (3D) printing has revolutionized the design and production of customized scaffolds, but the minimally invasive implantation of 3D-printed structures into the human body remains challenging. This has prompted the exploration of innovative materials and technical solutions. Shape-memory polymers, as advanced intelligent materials, exhibit considerable potential in minimally invasive surgical applications. Herein, we developed a novel thermosetting shape-memory polymer, poly(L-lactic acid)-trimethylene carbonate-glycolic acid (PLLA-TMC-GA), for the fabrication of bioengineered scaffolds with body temperature-activated shape-memory functionality. We comprehensively evaluated the mechanical properties, thermal stability, shape-memory capabilities, biocompatibility, biodegradability, and 3D printing performance of PLLA-TMC-GA terpolymers with various compositions. The results indicate that PLLA-TMC-GA exhibits exceptional shape-memory performance, adjustable material properties, favorable biocompatibility, and the potential for controlled biodegradation and reabsorption. The use of PLLA-TMC-GA as a biodegradable shape-memory polymer allows the reduction of implant volume, simplifies implantation, and enables on-demand activation at body temperature. These characteristics present new opportunities for the advancement of minimally invasive surgical techniques.

Xulin Hu and Jun Wang have contributed equally to this work.

✉ Xulin Hu
huxulin1993@163.com

✉ Shuai Li
allenle1991@sina.com

✉ Ning Hu
huncqjoint@yeah.net

[1] Clinical Medical College and Affiliated Hospital of Chengdu University, Chengdu 610081, China

[2] Department of Orthopedics, The First Affiliated Hospital of Chongqing Medical University, Chongqing 400042, China

[3] Department of Sports Medicine, The First Affiliated Hospital of Kunming Medical University, Kunming 650032, China

[4] Internal Medicine-Oncology, The First Affiliated Hospital of Kunming Medical University, Kunming 650032, China

[5] Department of Orthopedics, The First Affiliated Hospital, Zhejiang University School of Medicine, Hangzhou 310003, China

[6] State Key Laboratory of Biotherapy, West China Second University Hospital, Sichuan University, Chengdu 610041, China

Graphical abstract

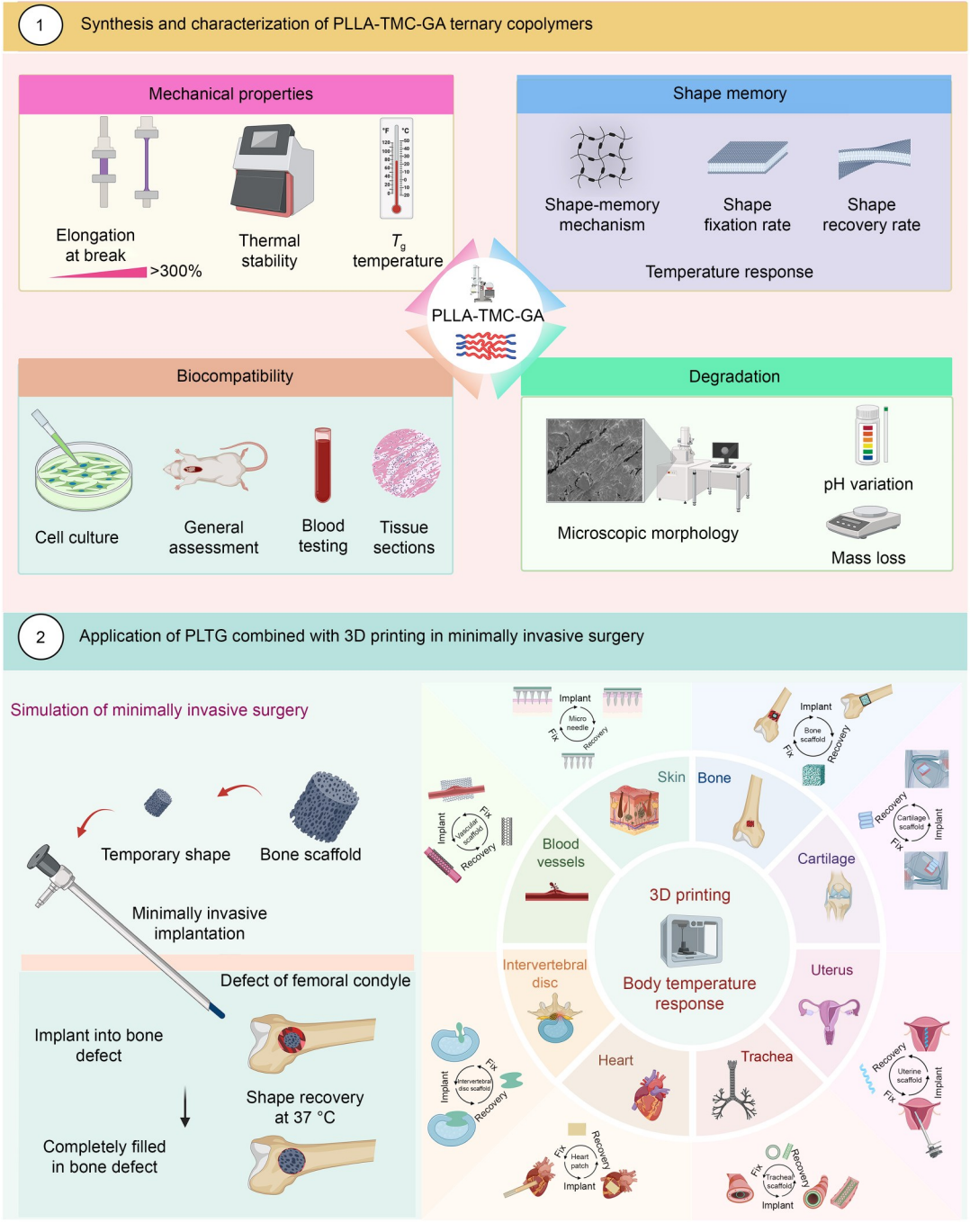

Keywords Biodegradable polymers · Shape-memory polymers · 3D printing technology · Biocompatibility · Tissue engineering applications

1 Introduction

Modern medicine aims to treat diseases while preserving organ structures, striving to restore patients to their pre-illness health. However, traditional surgeries often alter human anatomy and reconstruct organs, negatively impacting patients' postoperative quality of life [1]. Minimally invasive surgery (MIS) has become the dominant approach in

surgery because of its multiple benefits: reduced trauma and postoperative pain, shorter hospital stay, quicker recovery, better aesthetics, and lower infection rates [2, 3].

However, MIS still faces notable challenges, such as limited instrument range and restricted surgical field visibility, which can complicate implant placement [4, 5]. However, whereas metallic implants are nondegradable and can induce inflammatory responses [6], biodegradable materials offer enhanced tissue compatibility and natural absorption by the body, reducing the need for follow-up surgeries [7]. Biodegradable shape-memory polymers (BSMPs) offer additional benefits of compact size, programmable nature, and natural absorption by the body [8]. These materials have demonstrated efficacy in various medical applications, including tissue regeneration, implant technology, and drug delivery systems [9, 10].

The trigger temperature and energy density of BSMPs are crucial for their practical application in biomedicine and smart sensing. Therefore, the development of thermally responsive shape-memory polymers (SMPs) with ideal trigger temperatures (25–37 °C) [11] and high energy density is considered the most promising research direction [12]. Poly(L-lactic acid) (PLLA), a primary temperature-responsive SMP material [13–15], shows promising shape-memory characteristics but faces two main challenges that limit its application scope in the biomedical field: acidic degradation products and excessive rigidity [16]. The incorporation of polytrimethylene carbonate helps address these issues by enabling neutral degradation, thereby reducing inflammatory responses. Further introduction of glycolic acid (GA) units into PLLA-1,3-trimethylene carbonate (TMC) can disrupt the regularity of the PLLA-TMC molecular chain structure, thereby reducing the crystallinity, increasing the toughness, regulating the shape recovery temperature, enhancing the recovery deformation, and accelerating the degradation rate of the resulting implants [17].

Herein, we synthesized PLLA-TMC-GA (PLTG) terpolymers with different compositions through the ring-opening polymerization of L-lactic acid (LLA), TMC, and GA with stannous octanoate ($Sn(Oct)_2$) as the catalyst. We synthesized three distinct terpolymers with specific LLA/TMC/GA feed molar ratios: 63:27:10, 56:24:20, and 49:21:30, labeled PLTG10, PLTG20, and PLTG30, respectively. We characterized the structure of the synthesized terpolymers using gel permeation chromatography (GPC), Fourier transform infrared (FTIR) spectroscopy, ^{1}H nuclear magnetic resonance (NMR), and X-ray diffraction (XRD) analysis, and examined their thermal and mechanical properties through dynamic mechanical analysis (DMA) and universal mechanical testing. We assessed their shape-memory performance by measuring the shape fixity and recovery capabilities. We evaluated the biocompatibility of the terpolymers through in vitro cell studies and in vivo subcutaneous implantation tests, analyzing the degradation patterns and immunological responses. The present study explores the potential of PLTG terpolymers as 3D printable materials for MIS applications.

2 Experimental section

2.1 Materials

LLA (purity: 99%), TMC (purity: 99%), and GA (purity: 99%) were purchased from the Chinese Academy of Sciences. Stannous octoate ($Sn(Oct)_2$; purity: 99%) used as the catalyst was procured from Aladdin (Shanghai, China). Chloroform (purity: 99%), methanol (purity: 99%), and other reagents were obtained from Sinopharm Chemical Reagent Co., Ltd. (China). The reagents used in the cell experiments were purchased from HyClone (Logan, USA).

2.2 Synthesis of PLTG and its analysis

Polymerization. Details are provided in Sect. S2.2 in the supplementary information.

^{1}H NMR. ^{1}H NMR was used to determine the composition and microstructure of the terpolymers. ^{1}H NMR spectra were recorded at room temperature using a 400-MHz Bruker spectrometer with deuterated chloroform ($CDCl_3$) as the solvent.

GPC. Agilent PIGPC220 (USA) was used to determine the relative molecular weight. Dichloromethane served as the mobile phase, with a flow rate of 1 mL/min and an injection volume of 20 μL.

XRD. XRD (DX-2700BH, HAOYUAN, Liaoning, China) with Cu Kα radiation (wavelength λ=0.154 nm) was used to analyze the crystallinity of PLTG. Scanning was performed in a range of 2θ=10°–90° at a scanning speed of 4 (°)/min.

FTIR spectroscopy. An attenuated total reflection FTIR spectrometer (FTIR-650S, Suzhou Fubaiter Instrument Technology Co., Ltd., China) was used to analyze the chemical structure of PLTG. To comprehensively evaluate the molecular composition of the samples, the measurement range was set to 500–4000 cm^{-1}.

Differential scanning calorimetry (DSC). DSC was performed using an MT823e instrument (Mettler Toledo, Ohio, USA) in a nitrogen environment as follows: First, the sample was heated from − 50 to 220 °C at a rate of 10 °C/min and was held at 220 °C for 1 min to eliminate the thermal history. Subsequently, the sample was cooled to − 50 °C at a rate of 10 °C/min and was heated again to 220 °C at the same rate. The glass transition temperature was determined during the second heating scan.

Thermogravimetric analysis (TGA). The thermal stability of the terpolymers was evaluated using a TG 209 F3 thermal analyzer (Netzsch, Germany). The experiment was conducted in a nitrogen atmosphere, using a temperature range

of 40 – 800 °C and a heating rate of 20 °C/min. The mass change of the materials at different temperatures was determined, indicating their thermal stability.

DMA. DMA was performed using a DMA-Q800 (TA Instruments, USA). The test was conducted in the tensile mode, with the storage modulus, loss modulus, and loss factor of PLTG being evaluated. Dynamic temperature scanning was performed under the following conditions: strain of 0.1%, frequency of 1 Hz, preloading of 0.01 N, heating rate of 5 °C/min, and a temperature range from − 80 to 100 °C. The dimensions of the test samples were approximately 12 mm×4 mm×0.5 mm.

Time-dependent water contact angle. An optical tensiometer (Theta Lite, Biolin Scientific, Finland) was used to measure the time-dependent water contact angle. Using a pipette, a droplet of distilled water was placed on the PLTG film at 20 °C, and images of the surface were captured at different time points. To ensure data reliability and representativeness, we averaged the results from three independent experiments to assess the trend in the water contact angle over time.

Atomic force microscopy (AFM). Details are provided in Sect. S2.2 in the supplementary information.

Mechanical testing. The mechanical properties of the PLTG samples were evaluated using an electronic universal testing machine (MTS-C43.104Y, MTS Systems, USA) at two temperatures, 20 and 37 °C, with the tensile rate set to 10 mm/min. Through these tests, we obtained the stress–strain curves, tensile strength, and elongation at break data for PLTG. PLTG films (0.1 mm thick) were fabricated through solution evaporation and cut into dumbbell-shaped samples conforming to the GB/T 528-2009 standard, with dimensions of approximately 20 mm×5 mm×0.1 mm. To ensure data reliability and representativeness, we conducted three independent tests and used their average as the final mechanical performance evaluation result.

Thermal-induced shape-memory behavior. PLTG films (0.6-mm thick) were fabricated through solution evaporation. We conducted a quantitative study on the shape-memory capability of PLTG films via the folding–unfolding method. First, the PLTG strips were heated in a 37 °C water bath and deformed to a set deformation angle (θ_d). Next, under external stress, the samples were cooled in 0 °C water to fix the bent shape. After the stress was removed, the bent samples were maintained at a fixed angle (θ_f). Subsequently, they were reheated to 37°C, recovering to a recovery angle (θ_r). The shape fixation ratio (R_f) and shape recovery ratio (R_r) were calculated using the following formulas:

$$R_f = (\theta_f / \theta_d) \times 100\%, \quad (1)$$

$$R_r = (\theta_f - \theta_r)/\theta_f \times 100\%. \quad (2)$$

Details on the experimental methods are provided in Sect. S2.2 in the supplementary information.

In vitro degradation. Details on the in vitro hydrolytic and enzymatic degradation experiments are provided in Sect. S2.2 in the supplementary information.

The degradation metrics, including the mass loss (W_L) and water absorption rate (r_{wa}), were calculated as follows:

$$W_L = (W_i - W_d)/W_i \times 100\%, \quad (3)$$

$$r_{wa} = (W_w - W_d)/W_i \times 100\%, \quad (4)$$

where W_i, W_w, and W_d denote the initial mass, wet postdegradation mass, and dry mass of the film samples, respectively. Data were collected from three parallel experiments, with pH measurements conducted at specific intervals via a METTLER TOLEDO FiveEasy^{TM} Plus pH meter (Switzerland). The microstructural evolution of PLTG during degradation was investigated using scanning electron microscopy (SEM). The samples were sputter-coated with gold using a Leica EM ACE200 (Germany) device before examination using an AMRAY 1000B SEM (USA) at 20 kV. This methodology enabled the comprehensive investigation of surface morphological alterations throughout degradation.

2.3 Cytotoxicity assay

The details on cell culture, cell counting kit-8 (CCK-8), calcein acetoxymethyl ester/propidium iodide (Calcein-AM/PI), scratch assay, Transwell assay, and colony formation assay are provided in Sect. S2.3 in the supplementary information.

2.4 In vivo biocompatibility test

Detailed information regarding sample collection and analysis methods in animal experiments is provided in Sect. S2.4 in the supplementary information.

2.5 Rheological analysis

All rheological experiments were conducted on an MCR302 hybrid rheometer (Shanghai Baosheng, China) with temperature control, using an 8-mm stainless steel parallel plate maintained at 25 °C. The frequency sweep analysis was conducted via angular frequency scans (0.159–159 Hz) on three PLTG inks at 25 °C under 100 Pa stress to determine the dependences of the storage modulus (G') and the loss modulus (G'') on the angular frequency. In the dynamic oscillatory strain experiments, we measured G' and G'' versus time at 1% and 100% oscillatory strain (γ) at a constant frequency of 1 Hz. We also measured the shear stress/viscosity as a function of the shear rate at rotational shear rates of 0–100 s^{-1}.

2.6 3D printing

Printing was performed using a 3D bioprinter (EFL-BP-6601, EFL-Tech (Suzhou) Co., Ltd., China). All 3D models were designed using 3ds Max software. PLTG was combined with dioxane at a mass-to-volume ratio of 1:4 – 1:6 (g:mL) and

stirred magnetically for 6 h. The bioink was then printed layer by layer using a low-temperature deposition 3D printer with the following parameters: layer thickness of 400 μm, travel speed of 25 mm/s, printing speed of 7 mm/s, retraction speed of 10 mm/s, nozzle temperature of 25 °C, and platform temperature of −5 °C. The printed scaffolds were freeze-dried in a lyophilizer (Alpha-2-LDplus, Martin Christ, Germany) for 48 h and then dried in a vacuum oven at 37 °C for 7 d to remove the residual solvent [18].

2.7 Statistics and reproducibility

The data are presented as mean±standard deviation from at least three independent experiments. Statistical analysis was performed using GraphPad Prism software (version 10). Statistically significant differences between two groups were determined via *t*-tests, and differences among multiple groups were assessed via one-way analysis of variance. $p<0.05$ was considered statistically significant.

3 Results and discussion

3.1 Synthesis and performance analysis of the PLTG terpolymers

3.1.1 Synthesis of PLTG

Herein, PLTG terpolymers were synthesized using controlled polymerization reactions. Specifically, ring-opening copolymerization with $Sn(Oct)_2$ as catalyst was employed (detailed methods are provided in Sect. S2.2 in the supplementary information). The yields of PLTG10, PLTG20, and PLTG30 were 89%, 85%, and 86%, respectively. The synthesis pathway is shown in Fig. 1a [17].

3.1.2 Characterization of PLTG

Figure 1b presents the ^{1}H NMR spectra of the PLTG terpolymers. The LLA unit exhibited characteristic peaks at 5.17 ppm (peak 1; 1 ppm≈600 Hz) and 1.56 ppm (peak 5). The TMC main chain showed peaks at 2.01 ppm (peak 4) and 4.21 ppm (peak 3), and the GA unit exhibited multiple peaks (peak 2). Analysis of the peak areas confirmed that the composition of the polymers closely matched the initial feed ratio (Fig. S1 and Table S1 in the supplementary information). GPC showed a single peak, indicating a uniform molecular weight distribution (Fig. S2 in the supplementary information). The determined key metrics, including the number average molecular weight (M_n), the weight average molecular weight (M_w), and polydispersity index (PDI), are presented in Table S1 (supplementary information), showing that the M_w of the PLTG samples ranges from 1.0×10^4 g/mol to 2.0×10^4 g/mol. XRD analysis revealed the amorphous nature of PLTG, as shown by the absence of diffraction peaks (Fig. 1c). Figure 1d shows the FTIR spectra of the PLTG terpolymers, exhibiting characteristic peaks at 1752 cm^{-1} (C=O stretching), 1187 cm^{-1} (−C−C−O stretching), 1086 cm^{-1} (C−O stretching), 1275 cm^{-1} (O–C–O), 1368 cm^{-1} (PLLA methane), 1455 cm^{-1} (PGA CH_2), and 865 cm^{-1} (C–C stretching).

Figure 1e shows the DSC reheating curves for PLTG with various monomer ratios. Each curve exhibited a single glass transition, confirming that PLTG has a random copolymer structure. The addition of TMC and GA reduced the crystallinity of PLTG20 terpolymers, resulting in a melting temperature (T_m) of 95.37 °C and an enthalpy change (ΔH) of 0.788 J/g. Although PLTG10 has a higher LLA content, its lower T_m and ΔH values indicated reduced molecular chain order and shorter LLA segment length. This trend showed that an increase in TMC content or a decrease in LLA content led to a lower glass transition temperature (T_g). The TGA results indicated that the terpolymers are thermally stable below 200 °C and decompose in a single stage. The decomposition temperature (T_d) for all ternary copolymers exceeded 300 °C, making them suitable for biomedical applications. However, owing to their random chain structure, their overall thermal stability was lower than that of PLLA or PGA.

DMA was performed to examine the viscoelastic behavior and shape-memory properties of the terpolymers by measuring the storage modulus and loss factor (Fig. 1g; Fig. S4 in the supplementary information). Below T_g, PLTG20 and PLTG30 showed higher elastic moduli than PLTG10. However, above room temperature, PLTG10 exhibited a higher storage modulus than PLTG30, likely because of stronger interactions between polymer chain segments. The activation of shape memory occurred above T_g; consequently, the storage modulus at elevated temperatures directly correlated with the shape recovery capability—a higher storage modulus above T_g indicated a stronger shape recovery force.

The synthesized PLTG terpolymers exhibited lower surface contact angles (77.4°–82.5°) than PLLA (85.2°), suggesting that the incorporation of TMC and GA slightly increased hydrophilicity (Fig. S5 in the supplementary information). Nevertheless, all the synthesized polymers were hydrophobic. AFM results indicated that the surface roughness increased with TMC and GA contents (Fig. S6 in the supplementary information). Figure 1h shows the stress−strain behavior of the terpolymers at room temperature (20 °C) and body temperature (37 °C). To investigate the compressive properties of the prepared materials, we tested 3D-printed square scaffolds (10 mm×10 mm×6 mm, 70% porosity). Figure S7 (supplementary information) shows distinct compressive behaviors of the PLTG terpolymers with different compositions, with the compression modulus decreasing with the increase in the GA content. The results of mechanical tests (Figs. 1i and 1j) revealed that irrespective of the testing temperature, the elongation at break of PLTG increased, the tensile strength slightly decreased, and the elasticity and

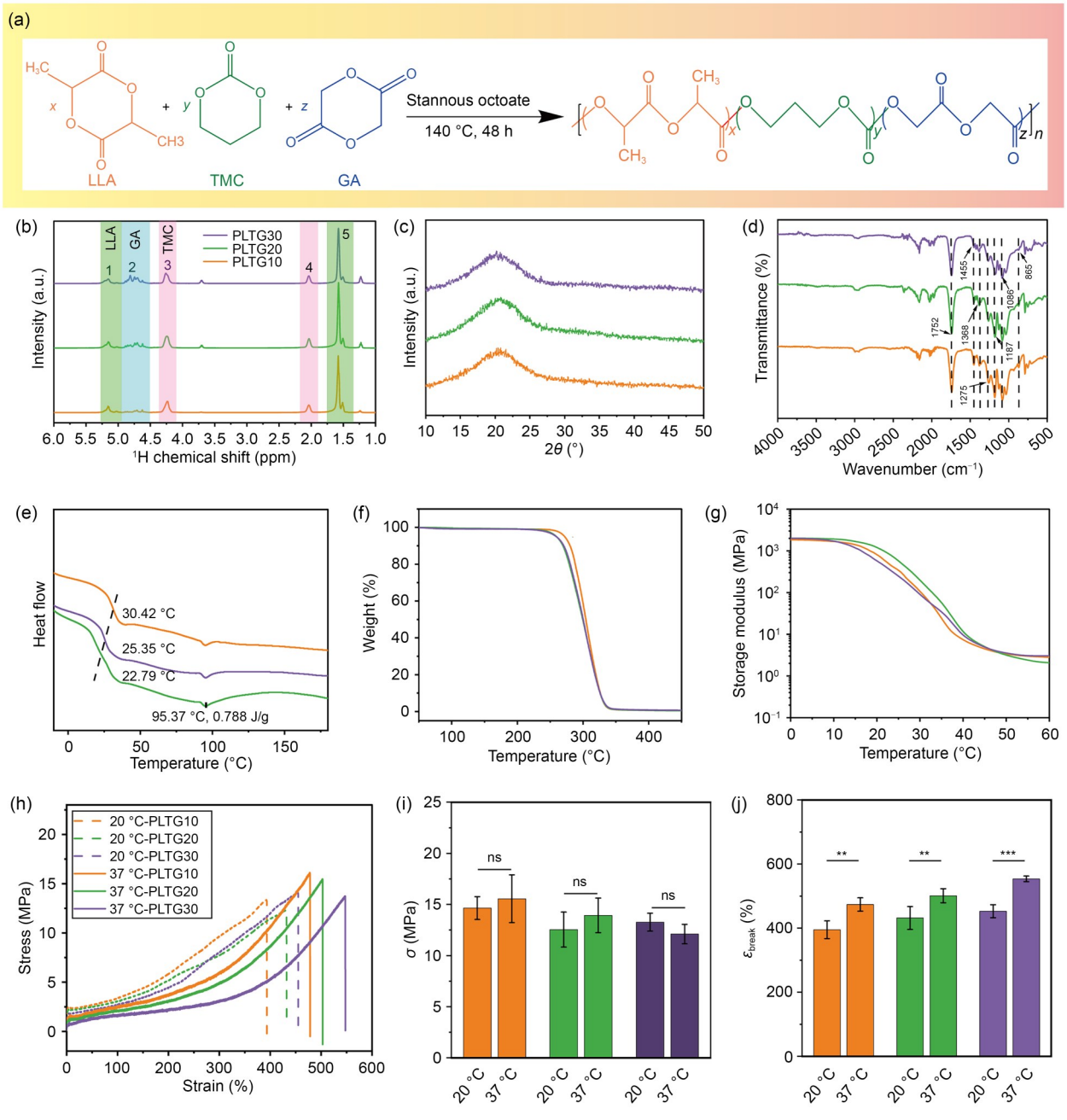

Fig. 1 Synthesis and physicochemical properties of the PLTG terpolymers. (a) Synthesis of PLTG. NMR spectra (b), XRD patterns (c), FTIR spectra (d), DSC curves (e), TGA curves (f), and DMA results (g) for PLTG10, PLTG20, and PLTG30. (h) Stress–strain curves for PLTG10, PLTG20, and PLTG30 at 20 and 37 °C. Tensile strength (i) and elongation at break (j) of PLTG10, PLTG20, and PLTG30 measured at 20 and 37 °C. Data are expressed as mean±standard deviation (n=3); $^{**}p$<0.01, $^{***}p$<0.001; ns: not significant. 1 ppm≈600 Hz

toughness of PLLA markedly increased with increasing LLA content and decreasing GA content. This was attributed to the crystallinity and mechanical strength of each component segment in the polymer.

3.2 Shape-memory properties

The shape-memory characteristics of BSMPs depend on two types of networks: permanent networks (stable cross-links) and temporary networks (reversible physical cross-links) [19]. Permanent networks enable shape recovery using stored elastic energy, whereas temporary networks maintain the deformed shape until triggered [20]. As shown in Fig. S8a (supplementary information), temperature changes govern how these networks behave during shape programming and recovery.

The shape-memory performance of the synthesizer materials was evaluated using two metrics: the shape fixation

ratio (R_f) and the shape recovery ratio (R_r). The tests were performed at room temperature (20 °C) and body temperature (37 °C). At room temperature, PLTG20 and PLTG30 exhibited relatively low shape fixation ratios. However, at 37 °C, all samples showed excellent shape recovery ratios, exceeding 99% (Fig. 2b; Fig. S8b in the supplementary information). Because of their lower glass transition temperatures (T_g), PLTG20 and PLTG30 underwent spontaneous deformation at room temperature, resulting in reduced shape fixation ratios (Fig. 2a; Fig. S8b in the supplementary information).

3.3 In vitro degradation and morphological analysis

Hydrolysis is a key mechanism of the breakdown of biodegradable polymers in vivo [21]. During this process, polymer chains break apart, leading to a reduction in molecular weight and the formation of water-soluble substances [20]. These substances then enter bodily fluids where cells absorb them [22]. Specifically, biodegradable materials degrade through three hydrolytic mechanisms: main-chain hydrolysis producing low-molecular-weight products, side-chain

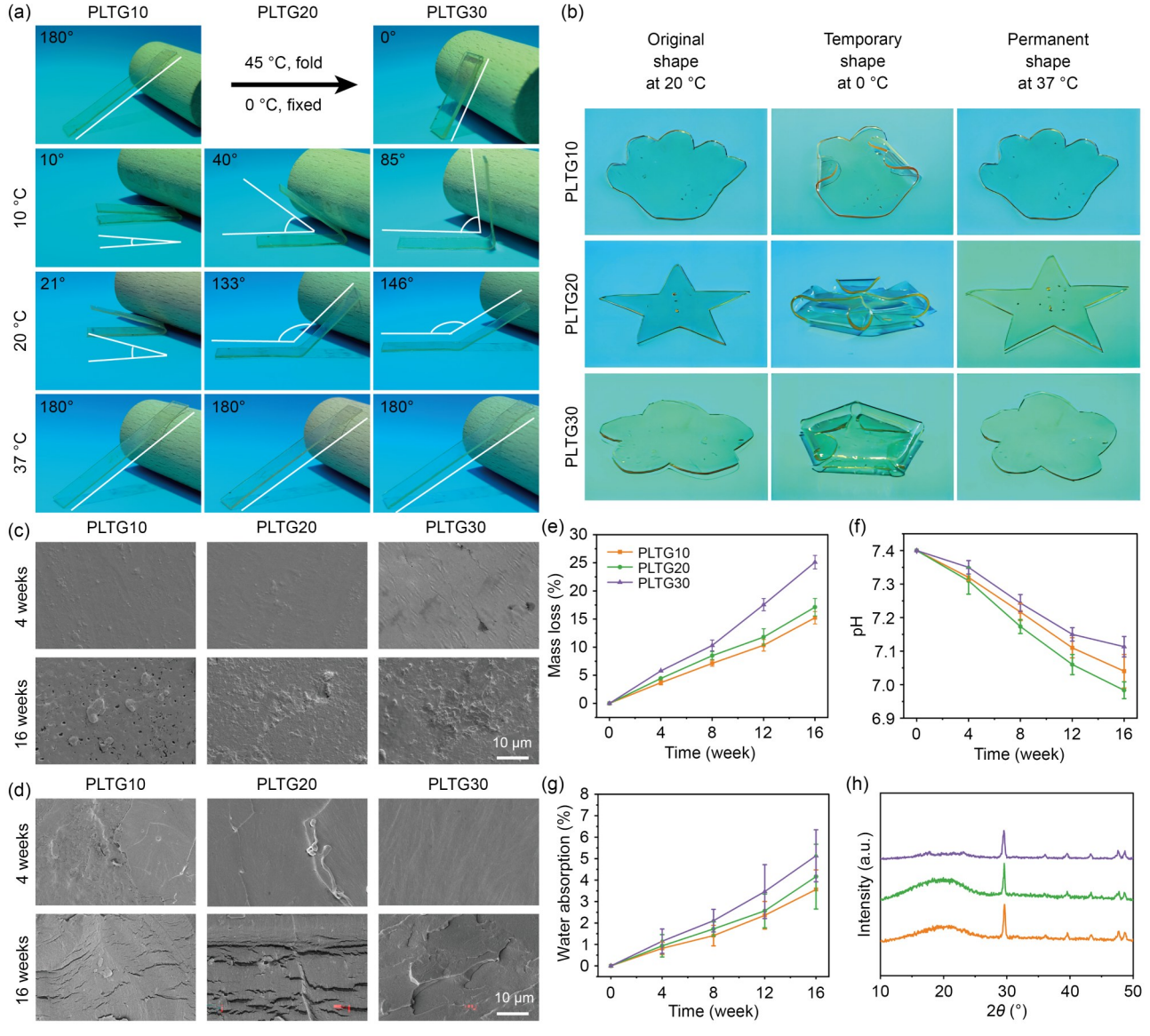

Fig. 2 Shape-memory behavior during in vitro degradation. (a) Shape fixation ratio and shape recovery ratio calculated based on the bending angles of PLTG strips at different temperatures. (b) Shape-memory behavior of PLTG sheets of different shapes at 37 °C. (c) SEM images of the surface of PLTG at specified time points (4 and 16 weeks) during hydrolysis (1000× magnification; scale bar: 10 μm). (d) SEM images of PLTG sections at specified time points (4 and 16 weeks) during hydrolysis (1000× magnification; scale bar: 10 μm). (e) Mass loss of the PLTG terpolymers during hydrolysis at 4, 8, 12, and 16 weeks. (f) pH value changes of the PLTG terpolymers during hydrolysis at 4, 8, 12, and 16 weeks. (g) Water absorption of the PLTG terpolymers during hydrolysis at 4, 8, 12, and 16 weeks. (h) XRD patterns of PLTG films after the 16-week degradation period. Data are expressed as mean±standard deviation (n=3)

hydrolysis yielding water-soluble polymers, and cross-link cleavage generating soluble linear polymers. To understand how the contents of TMC and GA affect PLTG degradation, we analyzed the surface microstructure, crystallization, mass reduction, and pH changes during in vitro hydrolysis.

SEM results revealed morphological changes in the three PLTG terpolymers over 16 weeks of hydrolysis. As shown in Fig. 2c and Fig. S9 (supplementary information), the surface of the terpolymers remained smooth for the first 4 weeks before developing erosion by week 8, with PLTG30 exhibiting the most severe degradation and PLTG10 the least. During weeks 12–16, crystal-like structures, pores, and sagging patterns were formed on the surfaces owing to the dissolution of amorphous regions. The cross-sectional morphology (Fig. 2d; Fig. S9 in the supplementary information) revealed crack formation at week 12 owing to water penetration. However, even PLTG terpolymers with high LLA content showed faster bulk erosion than pure PLLA.

Figure 2e shows the mass loss patterns of the PLTG samples. Higher TMC and GA contents led to increased mass loss rates because of decreased crystallinity. After 16 weeks, PLTG30 exhibited the highest mass loss ((25.12±1.21)%), followed by PLTG20 ((17.12±1.56)%) and PLTG10 ((15.23±1.11)%). In the enzymatic degradation tests, all samples degraded more rapidly than they did in the hydrolysis tests, with PLTG30 achieving near-complete degradation at 24 weeks (Fig. S10 in the supplementary information). Increased LLA content improved the organization of molecular chains, forming crystalline regions that better resisted water penetration. At the same time, GA units accelerated the degradation of PLTG by disrupting the chain structure. Due to the presence of TMC and GA, PLTG materials maintained a pH above 7.0 (Fig. 2f), thus minimizing inflammatory responses [23]. Additionally, the terpolymers maintained moderate water absorption levels throughout the test, showing below 6% water absorption after 16 weeks (Fig. 2g).

XRD patterns obtained throughout hydrolytic degradation showed sharp diffraction peaks (Fig. 2h), indicating the crystallinity of degradation products. Notably, the LLA content was positively correlated with the crystallization tendency during degradation. Spectral peak area analysis revealed varying degradation rates among the components (Figs. S11a and S11b in the supplementary information). GPC analysis showed a uniform molecular weight distribution (Fig. S11c in the supplementary information), providing M_n, M_w, and PDI values during degradation (Table S2 in the supplementary information). FTIR results showed minimal structural changes (Fig. S11d in the supplementary information).

3.4 In vitro biocompatibility

An ideal biocompatible implant should seamlessly integrate with the host tissue, without eliciting an immune response. To evaluate the cellular biocompatibility of the three synthesized terpolymers, we performed CCK-8 assays, live/dead cell staining, cell scratch tests, colony formation assays, and Transwell experiments using both extraction solutions (see Sect. S2.3 in the supplementary information), revealing no statistically significant differences between the two extraction methods. The CCK-8 results showed that the three terpolymers did not significantly affect cell proliferation (Fig. 3a). Live/Dead cell staining tests indicated that all three terpolymers maintained high cell viability (Fig. 3b). The results of scratch, clone, and Transwell experiments (Figs. 3c–3e) further confirmed that PLTG did not affect cell migration or proliferation, with no significant differences observed between the blank control and treatment groups. In summary, all three PLTG terpolymers exhibited excellent cell compatibility and preserved cellular activity.

3.5 In vivo biocompatibility and degradation assessment

We assessed the degradation properties, the clinical pathology, biocompatibility, and systemic toxicity of PLTG sheet implants through a 16-week in vivo study in rats. In addition, we evaluated the immune modulation behavior in vivo (Fig. 4a). Blood cell count monitoring was used to detect inflammatory responses and assess immune function. Results showed that blood cell counts (red blood cells, white blood cells, and platelets) were within normal ranges for Sprague–Dawley (SD) rats (6.06×10^6–8.74×10^6, 3.99×10^3–10.47×10^3, and 4.36×10^5–8.44×10^5, respectively), with no significant differences between materials (Table S3 in the supplementary information) [24].

3.5.1 In situ and ex vivo degradation and inflammation assessment

A rat subcutaneous implantation model was used to evaluate the biocompatibility and degradation of the prepared terpolymers. During the 16-week follow-up period, no complications or signs of inflammation were observed (Fig. 4c). The results of enzyme-linked immunosorbent assay (ELISA) showed undetectable levels of IL-6 and TNF-α, and statistically similar IFN-γ and IL-10 levels between the experimental and control groups (Figs. 4d and 4e).

Ex vivo SEM images (Fig. 4b) showed that the surface morphology became progressively irregular over time, with pores larger than those initially observed in vitro. Materials with higher GA content exhibited more pronounced surface collapse because the rough surface facilitated the attachment of the fibrin matrix and cell migration during degradation [25]. Enzymatic degradation occurred more rapidly in vivo than in vitro, resulting in 16-week mass losses of (35.34±1.22)% (PLTG30), (30.72±0.23)% (PLTG20), and (25.08±1.45)%

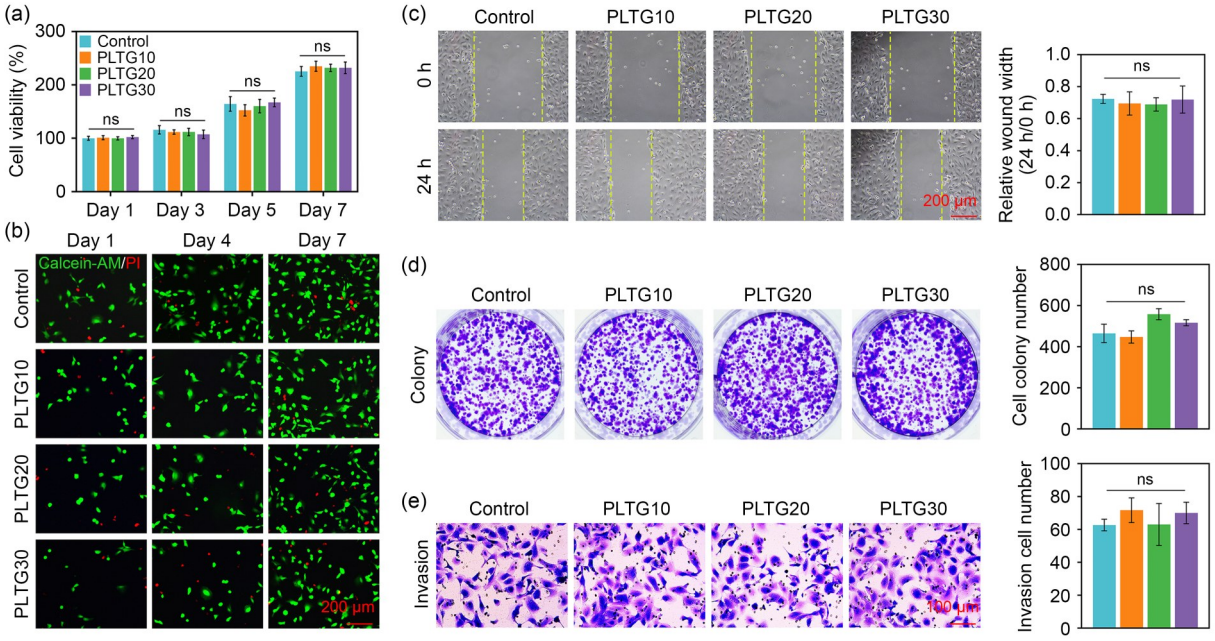

Fig. 3 In vitro evaluation of the biocompatibility of the PLTG membranes. (a) Cell viability assessed using the CCK-8 assay (1–7 d). (b) Inverted fluorescence microscopy images of human fibroblast cell line GM00526 (1, 4, and 7 d). (c) Cell migration analysis via scratch healing assay (0 and 24 h; scale bar: 200 μm). (d) Clonogenic formation efficiency after 7 d. (e) Transwell migration after 48 h (scale bar: 100 μm). Data are expressed as mean±standard deviation (n=3); ns: not significant

(PLTG10) (Fig. 4f). This trend aligns with that observed in the in vitro studies, where PLTG30 showed the fastest degradation and PLTG10 the slowest.

3.5.2 Inflammatory characteristics

Hematoxylin and eosin (H&E) staining was used to evaluate cell infiltration and the recruitment of inflammatory cells. After degradation, the implanted material triggered the formation of a fibrous capsule that encapsulates it. Therefore, the formation of a fibrous capsule was observed to assess the inflammatory response. At 2 months postimplantation, only a few fibrous capsules were observed around PLTG10/PLTG20/PLTG30. The dark-stained regions in the implants suggested slight calcification, but these regions did not cause an excessive inflammatory response. At 4 months postimplantation, no significant increase in capsule thickening and no notable inflammatory reaction were observed (Fig. 5a).

To assess the ability of the implants to recruit specific cells, immunohistochemical analysis was performed four months after implantation. Figures 5b–5g show minimal leukocyte differentiation antigen 3 (CD3) expression at all implantation sites, indicating no chronic inflammatory response. B lymphocytes (CD20) and macrophages (CD68) were evenly distributed in all cases, with PLTG30 samples showing a slightly greater, though not statistically significant, immune response. Notably, minimal quantities of M2 macrophages (CD163) and neutrophils (myeloperoxidase, MPO) were detected at all the implantation sites. Although the number of these cells slightly increases with TMC and GA contents, none of these differences reached statistical significance. These findings offer crucial insights into the complex interplay between implants and the host immune system, thereby enhancing our understanding of biomaterial-tissue interfaces [26].

3.5.3 Systemic evaluation: potential accumulation of material degradation products

To thoroughly assess the safety profiles of the prepared PLTG materials, we performed detailed pathological analyses of the major organs in the experimental rats, focusing on the heart, liver, spleen, lungs, and kidneys (Fig. S12 in the supplementary information). Four months postimplantation, comparative histopathological evaluations revealed no significant differences between the PLTG10, PLTG20, and PLTG30 groups and the control group, with no unusual pathological changes detected. These findings strongly suggest that the PLTG materials do not have any observable effects on the tissue architecture of these critical organs, confirming that the degradation products do not noticeably accumulate in the body.

3.6 Rheological characteristics of the PLTG bioinks

In bioprinting, it is crucial to achieve an optimal balance between the rheological properties of bioinks and the physicochemical attributes of the matrix during extrusion [27, 28].

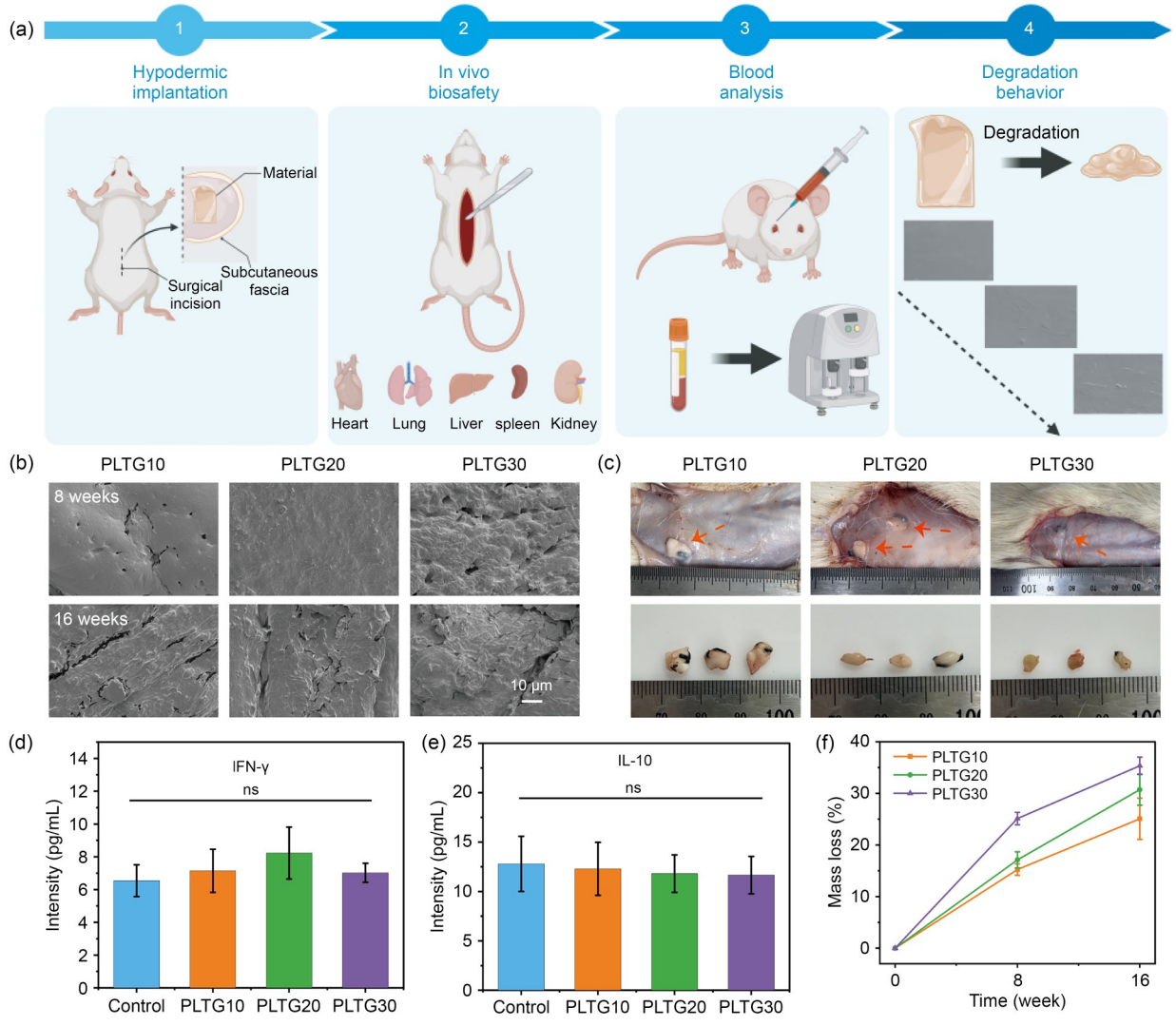

Fig. 4 In vivo assessment of the biocompatibility and degradation of the PLTG membranes. (a) Subcutaneous implantation in rats for biocompatibility assessment via histological, hematological, and degradation analyses. (b) SEM surface images at 8 and 16 weeks (1000× magnification; scale bar: 10 μm). (c) Macroscopic photographs showing the subcutaneous implantation sites of different PLTG materials in rats. Concentrations of IFN-γ (d) and IL-10 (e) in serum. (f) Mass loss during in vivo degradation. Data are expressed as mean±standard deviation (n=3); ns: not significant

An exemplary bioink would exhibit shear-thinning behavior, transitioning into a fluid-like state under high shear stress while retaining high viscosity under low shear stress or at rest [29].

We analyzed the PLTG bioinks with dioxane across different mass-to-volume ratios and temperatures. The optimal printing conditions were mass-to-volume ratios within the range of 1:4–1:6 and temperatures of 15–35 °C (Fig. 6a). At 15 °C, PLTG10 (PLTG to dioxane mass-to-volume ratio of 1:4) exhibited excessive viscosity, whereas PLTG30 (PLTG to dioxane mass-to-volume ratio of 1:6) showed insufficient viscosity at 35 °C, both compromising the print quality (Fig. 6b). The best results were achieved for PLTG10/PLTG20/PLTG30 (PLTG to dioxane mass-to-volume ratio of 1: 5) at 25 °C, showing consistent line width and ideal printing performance. Compared with conventional fused deposition manufacturing, low-temperature 3D printing offered multiple advantages. The lower processing temperature preserved the biological integrity of the materials. Additionally, the method enabled the printing of complex structures with interconnected macro- and micropores, improving scaffold porosity (Fig. 6c). This hierarchical structure optimized cellular nutrient exchange and diffusion. For bioinks suitable for direct-write extrusion 3D printing, specific viscoelastic properties were imperative. The key rheological parameters, including the loss factor tanδ (G''/G') and viscosity η, significantly affected the printing performance [30]. The results of frequency sweep analysis revealed that all PLTG bioinks were viscous fluids under dynamic conditions, facilitating high shape fidelity in extrusion-based 3D printing

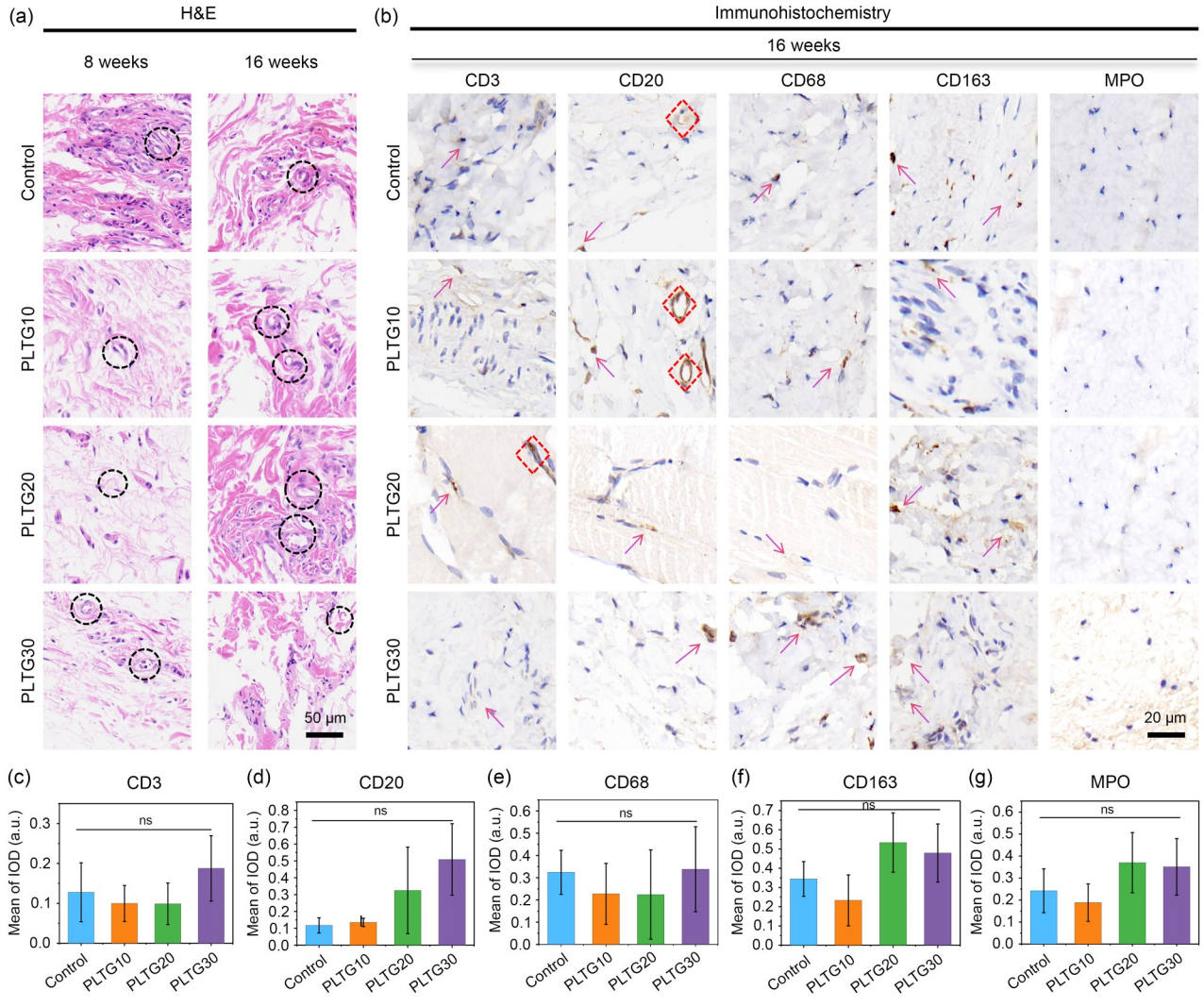

Fig. 5 Histological and immunohistochemical staining. (a) H&E-stained tissue evaluation of PLTG10, PLTG20, and PLTG30 implantation sites at 2 months and 4 months, with black circles indicating fibrous capsules (scale bar: 50 μm). (b–g) Representative images of immunohistochemical staining of the implanted materials at 4 months for CD3, CD20, CD68, CD163, and myeloperoxidase (MPO) (scale bar: 20 μm), with red diamonds indicating false positives caused by vesicles and arrows indicating true positives. Data are presented as mean±standard deviation (n=3); ns: not significant

(Fig. 6d). Dynamic oscillatory strain experiments indicated that under a constant frequency of 1 Hz, G' rapidly decreased at high strain (100%) in all formulations because of the shear-thinning effect; at the same time, upon returning to low strain (1%), G' nearly recovered to its initial value (Fig. 6e). The rotational shear rate sweep experiments further confirmed that the viscosity of all the tested bioinks decreased with increasing shear rate, indicating that the shear-thinning behavior was beneficial for pneumatic extrusion (Fig. 6f). However, it is important to note that an excessively low viscosity may result in filament spreading or collapse during printing.

Rheological data indicated that the increase in GA content led to decreases in the modulus and viscosity of the PLTG bioinks while the bioinks maintained compatibility with extrusion-based 3D printing. Therefore, at the optimal solvent ratio and printing temperature, these bioinks could achieve optimal shape fidelity and stacking performance for various applications.

3.7 Medical applications: exploring the potential of PLTG BSMPs in advanced 3D printing

Traditional 3D-printed scaffolds require extensive surgical exposure, necessitating the development of scaffolds that can be compactly inserted and can self-expand within the body. 3D-printed BSMP structures have recently driven notable advancements in MIS techniques [31]. These programmable structures are activated at body temperature, expanding to fill constricted areas and tissue voids [32]. Their excellent

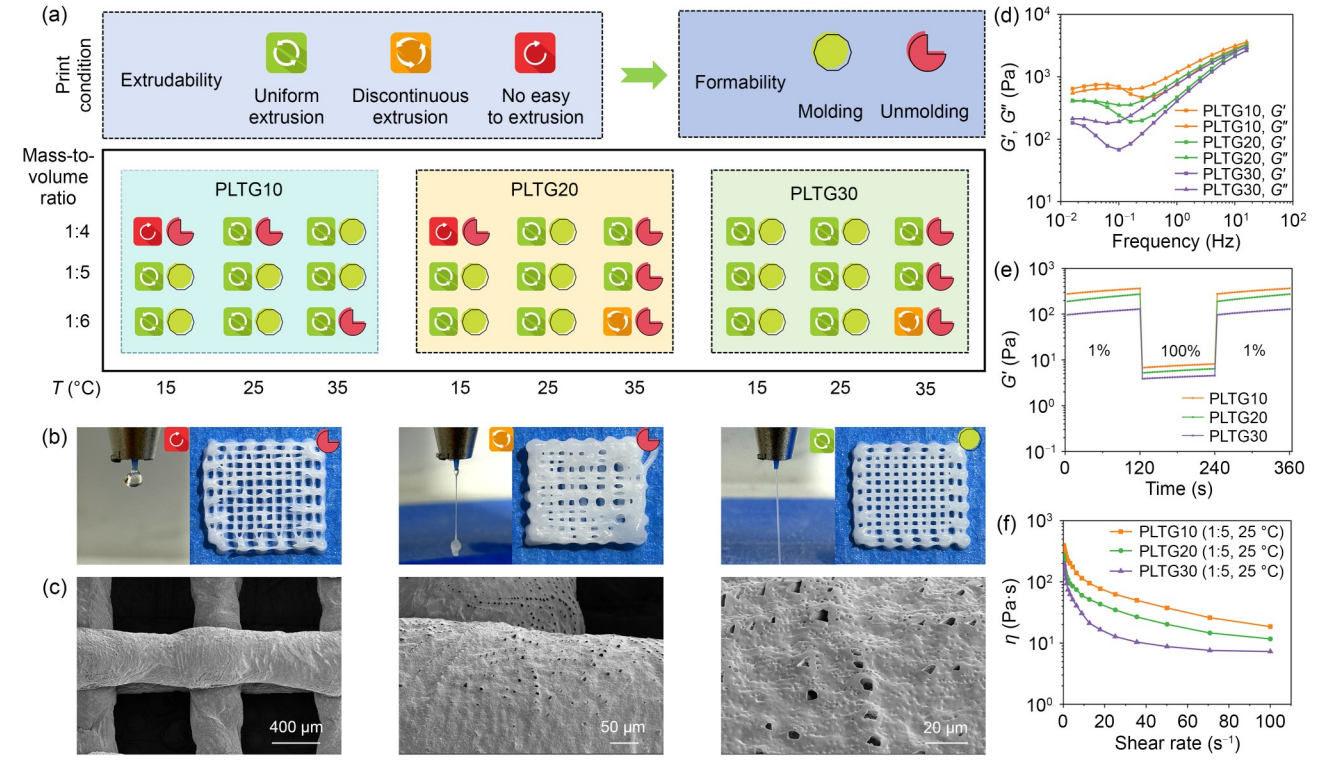

Fig. 6 Rheological properties and printing parameters of the PLTG bioinks. (a) Extrudability, formability, and printability of the PLTG bioinks. (b) Effects of solvent composition and temperature. (c) Micromorphology of bioscaffolds printed at low temperatures in dioxane. (d) Results of frequency sweep experiments conducted using printable PLTG inks. (e) Results of dynamic oscillatory strain experiments conducted using printable PLTG inks, with strain amplitude alternated between 1% and 100%. (f) Plot of viscosity versus shear rate for the printable PLTG bioinks, showing the shear-thinning behavior and the viscosity of each formulation. All figures presented represent the average of three independent tests

plasticity and mechanical properties make them invaluable for advanced medical applications [33].

Herein, we developed PLTG BSMPs to address the implantation challenges posed by the suboptimal transition temperatures (T_{trans}) of traditional SMPs. The prepared materials exhibited T_{trans} values of 20–37 °C, allowing shape programming at room temperature and subsequent transformation to the intended configuration in physiological environments. The 3D-printed structures fabricated from these materials showed exceptional shape memory capabilities. These scaffolds could be configured into the desired temporary forms at 0 °C, be implanted through minimally invasive channels, and rapidly recover their predetermined 3D structure at body temperature, ensuring precise alignment with the injured areas (Fig. 7a). They are particularly suitable for implantation into damaged tissues through restricted access points.

At physiological temperature (37 °C), PLTG showed optimal shape recovery, making it ideal for confined-space implantation. The superior rheological properties of the synthesized materials enabled the precise fabrication of complex 3D structures such as dumbbells, springs, folding fans, pipes, spider webs, and honeycombs. These 3D-printed biodegradable tissue engineering scaffolds exhibited uniformly interconnected porous structures, excellent biocompatibility, and intrinsic shape-memory capabilities at body temperature, excelling in MIS applications. To validate the 3D printing performance of PLTG, we fabricated a bioink by mixing PLTG20 and dioxane at a mass-volume ratio of 1:5. Using the optimized printing process (provided in Sect. 2.6), we successfully manufactured various tissue engineering scaffolds for different anatomical structures, including the uterine cavity, blood vessels, intervertebral discs, bones, and trachea (Fig. 7b) [34–36].

The integration of PLTG with 3D printing technology enabled the efficient and accurate development of personalized treatment strategies tailored to individual patients. The technology could considerably improve treatment outcomes and minimize patient discomfort. This innovative technology has a broad application potential and may catalyze a paradigm shift in personalized medicine, offering patients more precise and effective medical interventions.

4 Conclusions

Herein, we synthesized PLTG terpolymers with amorphous structures, excellent thermal stability, superior mechanical properties, and tunable degradation characteristics. The

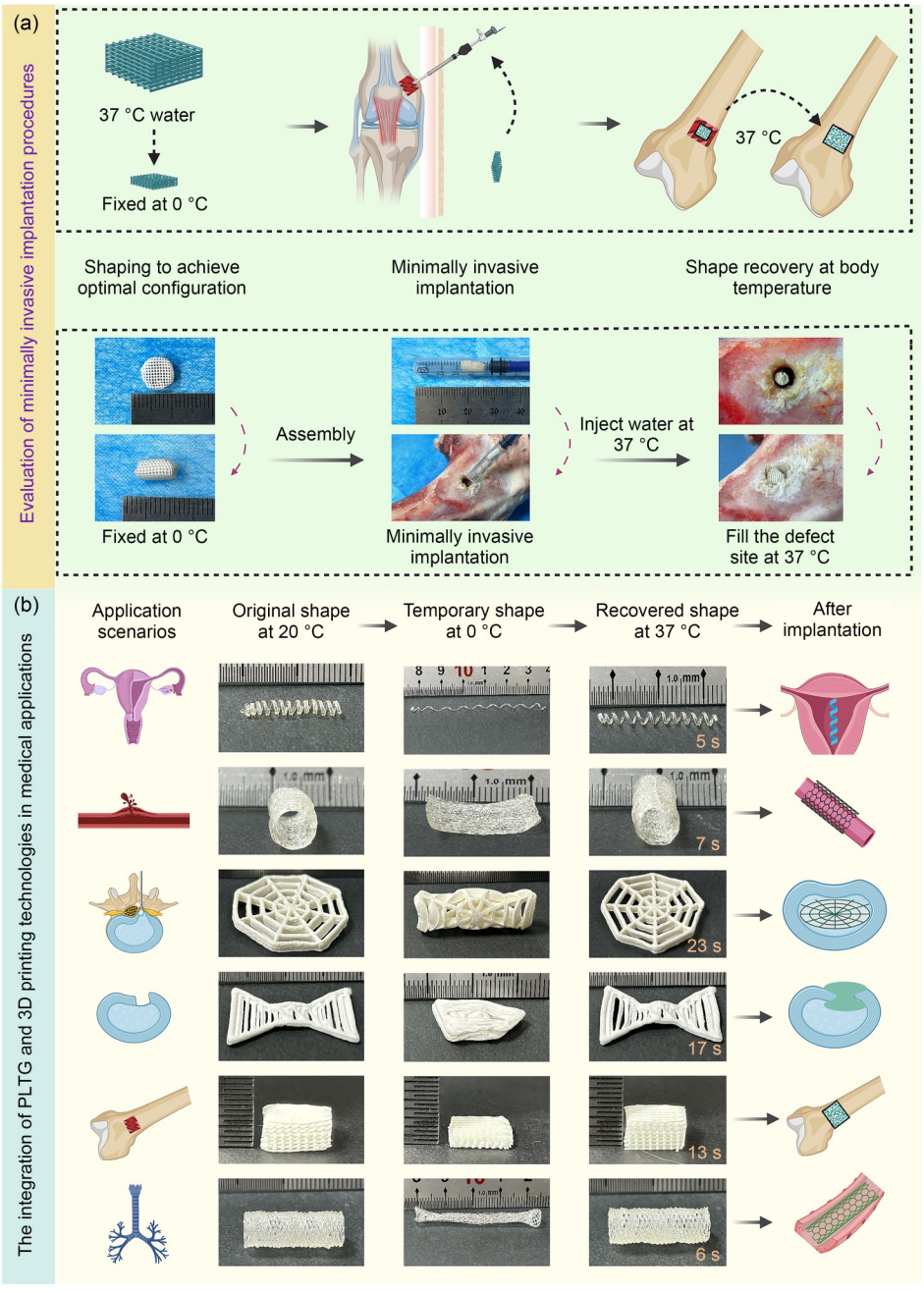

Fig. 7 Integration of PLTG and 3D printing in medical applications. (a) Evaluation of minimally invasive implantation procedures. (b) 3D-printed scaffolds and their potential biomedical applications; from left to right: initial configuration, temporary shape, and recovered shape, along with corresponding application scenarios (in the following order: uterine cavity, blood vessel, nucleus pulposus, annulus fibrosus, bone, and trachea)

rheological properties of the bioinks prepared from these terpolymers enabled the extrusion-based 3D printing of biological scaffolds with shape-memory functionality activated at body temperature. In vitro and in vivo studies confirmed the biocompatibility of PLTG, showing no inflammatory or toxic reactions. Additionally, the prepared materials showed optimal shape-memory properties at physiological temperature (37 °C). The combination of SMPs with 3D printing creates new opportunities for MIS, drug delivery, and tissue replacement. Although PLTG shows promise for customized medical implants, future research needs to address tissue-specific requirements and mechanical stability during degradation.

Supplementary Information The online version contains supplementary material available at https://doi.org/10.1631/bdm.2400486.

Acknowledgements This work was supported by the National Natural Science Foundation of China (Nos. 82402822, 82360427, 82372425, 82072443, and 32200559), the Priority Union Foundation of Yunnan

Provincial Science and Technology Department and Kunming Medical University (No. 202301AY070001-164), the Natural Science Foundation of Sichuan Province (No. 23NSFSC5880), and the Central Government of Sichuan Province Guiding the Special Project of Local Science and Technology Development (No. 2024ZYD0155). Graphical abstract and Fig. 7 were created using BioRender.

Author contributions XLH: writing–original draft, writing–review & editing, validation, supervision, project administration, methodology, investigation, formal analysis, data curation, conceptualization, and funding acquisition. JW: writing–original draft, writing–review & editing, validation, supervision, project administration, methodology, investigation, formal analysis, data curation, conceptualization, and funding acquisition. SHY: supervision, methodology, investigation, formal analysis, and data curation. JD: supervision, methodology, investigation, formal analysis, and data curation. WYF: supervision, methodology, investigation, formal analysis, and data curation. HMW: investigation, formal analysis, and data curation. DDH: investigation, formal analysis, and data curation. LLQ: investigation and formal analysis. JYY: investigation and formal analysis. ZGP: investigation and formal analysis. XY: investigation, formal analysis, and funding acquisition. YLL: investigation and formal analysis. SL: writing–original draft, writing–review & editing, investigation, and formal analysis. NH: writing–review & editing, project administration, and funding acquisition.

Declarations

Conflict of interest The authors declare that they have no conflict of interest.

Ethical approval All animal experiments complied with the experimental animal welfare ethics review of Sichuan University and were approved by the Institutional Animal Care and Use Committee of Chengdu Dossy Experimental Animals Co., Ltd. (Protocol number: YSY-DWLL-2023252).

Data availability The data that support the findings of this study are available from the corresponding authors upon reasonable request.

References

1. Linghu EQ (2024) New direction for surgery: super minimally invasive surgery. World J Gastroenterol 30(12):1676–1679. https://doi.org/10.3748/wjg.v30.i12.1676
2. Assem A, Hamdy SM, Beltagy AM et al (2021) Prospective evaluation of urinary continence after laparoscopic radical prostatectomy using a validated questionnaire and daily pad use assessment: which definition is more relevant to the patient's perception of recovery? Cent European J Urol 74(2):196–200. https://doi.org/10.5173/ceju.2021.0004.R1
3. Tesoro S, Gamba P, Bertozzi M et al (2022) Pediatric robotic surgery: issues in management-expert consensus from the Italian Society of Pediatric and Neonatal Anesthesia and Intensive Care (SARNePI) and the Italian Society of Pediatric Surgery (SICP). Surg Endosc 36(11):7877–7897. https://doi.org/10.1007/s00464-022-09577-0
4. Ri M, Ohashi M, Makuuchi R et al (2024) Clinical impact of polyglycolic acid mesh to reduce pancreas-related complications after minimally invasive surgery for gastric cancer: a propensity score matching analysis. J Gastric Cancer 24(2):220–230. https://doi.org/10.5230/jgc.2024.24.e17
5. Pushpanathan NR, Hashim MNM, Zahari Z et al (2022) Conversion rate and risk factors of conversion to open in laparoscopic appendicectomy. Ann Coloproctol 38(6):409–414. https://doi.org/10.3393/ac.2020.00437.0062
6. Qu XH, Yang HT, Jia B et al (2021) Zinc alloy-based bone internal fixation screw with antibacterial and anti-osteolytic properties. Bioact Mater 6(12):4607–4624. https://doi.org/10.1016/j.bioactmat.2021.05.023
7. Li XR, Deng QS, Liu PL et al (2024) Three-dimensional printed biomimetic multilayer scaffolds coordinated with sleep-related small extracellular vesicles: a strategy for extracellular matrix homeostasis and macrophage polarization to enhance osteochondral regeneration. VIEW 5(2):20230069. https://doi.org/10.1002/VIW.20230069
8. Zhang YC, Hu JL, Zhao X et al (2019) Mechanically robust shape memory polyurethane nanocomposites for minimally invasive bone repair. ACS Appl Bio Mater 2(3):1056–1065. https://doi.org/10.1021/acsabm.8b00655
9. Hussain M, Khan SM, Shafiq M et al (2024) Advances in biodegradable materials: degradation mechanisms, mechanical properties, and biocompatibility for orthopedic applications. Heliyon 10(12):e32713. https://doi.org/10.1016/j.heliyon.2024.e32713
10. Zhang H, Lin X, Cao XY et al (2024) Developing natural polymers for skin wound healing. Bioact Mater 33:355–376. https://doi.org/10.1016/j.bioactmat.2023.11.012
11. Liu B, Li H, Meng FZ et al (2024) 4D printed hydrogel scaffold with swelling-stiffening properties and programmable deformation for minimally invasive implantation. Nat Commun 15(1):1587. https://doi.org/10.1038/s41467-024-45938-0
12. An CH, Zhang Y, Guo HN et al (2019) Metal oxide-based supercapacitors: progress and prospectives. Nanoscale Adv 1(12):4644–4658. https://doi.org/10.1039/C9NA00543A
13. Aihemaiti P, Jia R, Aiyiti W et al (2023) Study on 3D printing process of continuous polyglycolic acid fiber-reinforced polylactic acid degradable composites. Int J Bioprint 9(4):734. https://doi.org/10.18063/ijb.734
14. Navaee F, Renaud P, Kleger A et al (2023) Highly efficient cardiac differentiation and maintenance by thrombin-coagulated fibrin hydrogels enriched with decellularized porcine heart extracellular matrix. Int J Mol Sci 24(3):2842. https://doi.org/10.3390/ijms24032842
15. Huang YQ, Zhao HX, Wang YX et al (2023) The application and progress of tissue engineering and biomaterial scaffolds for total auricular reconstruction in microtia. Front Bioeng Biotechnol 11:1089031. https://doi.org/10.3389/fbioe.2023.1089031
16. de Oliveira IR, Gonçalves IDS, Santos KWD et al (2023) Biocomposite macrospheres based on strontium-bioactive glass for application as bone fillers. ACS Mater Au 3(6):646–658. https://doi.org/10.1021/acsmaterialsau.3c00048
17. Li JF, Jiang PF, Yang JW et al (2024) Self-reinforced PTLG copolymer with shish kebab structures and a bionic surface as bioimplant materials for tissue engineering applications. ACS Appl Mater Interfaces 16(8):11062–11075. https://doi.org/10.1021/acsami.3c18093
18. Gill J, Gorlick R (2021) Advancing therapy for osteosarcoma. Nat Rev Clin Oncol 18(10):609–624. https://doi.org/10.1038/s41571-021-00519-8
19. Xu CC, Hong Y (2022) Rational design of biodegradable thermoplastic polyurethanes for tissue repair. Bioact Mater 15:250–271. https://doi.org/10.1016/j.bioactmat.2021.11.029
20. Salaris V, Leonés A, Lopez D et al (2022) Shape-memory materials via electrospinning: a review. Polymers 14(5):995. https://doi.org/10.3390/polym14050995
21. Lee JS, Kang SK (2021) Principles for controlling the shape

recovery and degradation behavior of biodegradable shape-memory polymers in biomedical applications. Micromachines 12(7):757. https://doi.org/10.3390/mi12070757
22. Ibrahim SW, Hamad TI, Haider J (2023) Biological properties of polycaprolactone and barium titanate composite in biomedical applications. Sci Prog 106(4):368504231215942. https://doi.org/10.1177/00368504231215942
23. Hu XL, Mi S, Lu JL et al (2021) In vitro degradation behavior of shape memory PLLA-TMC random copolymers. Colloids Surf A Physicochem Eng Aspects 615:126220. https://doi.org/10.1016/j.colsurfa.2021.126220
24. Valenzuela-Briseño AR, Arredondo-Damian JG, Rascón-Careaga A et al (2022) Hematologic evaluation of peripheral blood in Sprague Dawley rats by chronic exposure to aluminum chloride ($AlCl_3$). Environ Anal Health Toxicol 37(4):e2022034. https://doi.org/10.5620/eaht.2022034
25. Uesugi T, Shimoo Y, Munakata M et al (2024) A study of the associated risk factors for early failure and the effect of photofunctionalisation in full-arch immediate loading treatment based on the all-on-four concept. Bioengineering 11(3):223. https://doi.org/10.3390/bioengineering11030223
26. Moura D, Rohringer S, Ferreira HP et al (2024) Long-term in vivo degradation and biocompatibility of degradable pHEMA hydrogels containing graphene oxide. Acta Biomater 173:351–364. https://doi.org/10.1016/j.actbio.2023.11.012
27. Yin J, Zhao DK, Liu JY (2019) Trends on physical understanding of bioink printability. Bio-Des Manuf 2(1):50–54. https://doi.org/10.1007/s42242-019-00033-y
28. Zhang ZY, Jin YF, Yin J et al (2018) Evaluation of bioink printability for bioprinting applications. Appl Phys Rev 5(4):041304. https://doi.org/10.1063/1.5053979
29. Smith PT, Basu A, Saha A et al (2018) Chemical modification and printability of shear-thinning hydrogel inks for direct-write 3D printing. Polymer 152:42–50. https://doi.org/10.1016/j.polymer.2018.01.070
30. Gao T, Gillispie GJ, Copus JS et al (2018) Optimization of gelatin–alginate composite bioink printability using rheological parameters: a systematic approach. Biofabrication 10(3):034106. https://doi.org/10.1088/1758-5090/aacdc7
31. Upadhyay C, Ojha U (2023) Stress-induced shape-shifting materials possessing autonomous self-healing and scratch-resistant ability. Chem Asian J 18(4):e202201082. https://doi.org/10.1002/asia.202201082
32. Hu XL, Lin ZD, He J et al (2022) Recent progress in 3D printing degradable polylactic acid-based bone repair scaffold for the application of cancellous bone defect. MedComm Biomater Appl 1(1):e14. https://doi.org/10.1002/mba2.14
33. Mao ZN, Bi XW, Yu CH et al (2024) Mechanically robust and personalized silk fibroin-magnesium composite scaffolds with water-responsive shape-memory for irregular bone regeneration. Nat Commun 15(1):4160. https://doi.org/10.1038/s41467-024-48417-8
34. Hu XL, Zhao WM, Zhang Z et al (2023) Novel 3D printed shape-memory PLLA-TMC/GA-TMC scaffolds for bone tissue engineering with the improved mechanical properties and degradability. Chin Chem Lett 34(1):107451. https://doi.org/10.1016/j.cclet.2022.04.049
35. Hu XL, Chen J, Yang SH et al (2024) 3D printed multifunctional biomimetic bone scaffold combined with TP-Mg nanoparticles for the infectious bone defects repair. Small 20(40):2403681. https://doi.org/10.1002/smll.202403681
36. Hu XL, Yang SH, Zhao WM et al (2024) Novel multi-functional microsphere scaffold with shape memory function for bone regeneration. Biomater Adv 163:213958. https://doi.org/10.1016/j.bioadv.2024.213958